

Thermophysical property models for lunar regolith

Samuel S. Schreiner^{a,*}, Jesus A. Dominguez^{b,2}, Laurent Sibille^{b,3}, Jeffrey A. Hoffman^{a,4}

^a *Massachusetts Institute of Technology, 77 Massachusetts Avenue, Cambridge, MA 02139, United States*

^b *NASA Kennedy Space Center, FL 32899, United States*

Received 7 August 2015; received in revised form 19 November 2015; accepted 22 December 2015

Available online 29 December 2015

Abstract

We present a set of thermophysical property models for lunar regolith. Data from over 25 sources in the literature are integrated and fit with regression models for the following properties: composition, density, specific heat, latent heat of melting/fusion, thermal conductivity, electrical conductivity, optical absorption length, Gibbs Free Energy and Enthalpy of Formation. The models are based on data from Apollo samples and high-temperature molten regolith simulants, extending significantly beyond existing models in the literature. Furthermore, separate regression models are presented for Mare and Highlands regolith to demonstrate the effect of composition and to allow the models to be tailored to a wide range of applications. These models can enable more consistent, informed analysis and design of lunar regolith processing hardware and can also support lunar geological simulations. In addition to regression models for each material property, the raw data are presented to allow for further interpretation and fitting as necessary.

© 2016 COSPAR. Published by Elsevier Ltd. All rights reserved.

Keywords: Lunar regolith; Material property models; Electrical conductivity; Specific heat; Thermal conductivity; In Situ Resource Utilization

1. Introduction

Although the lunar surface missions during the Apollo and Luna programs brought over 380 kg of lunar samples to Earth, significant uncertainty remains concerning the material properties of lunar regolith. These uncertainties have often impeded rigorous engineering design and analysis of hardware designed to interact with lunar regolith, including reactors to perform In-Situ Resource Utilization (ISRU) (Linne, 2010; Schreiner et al., 2015), pneumatic

and mechanical regolith transport devices (Mueller et al., 2010; Standish, 2010), and regolith excavation devices (Zacny et al., 2009). Furthermore, uncertainty concerning regolith material properties affects simulations of lunar geological evolution (Snyder et al., 1994) and predictions of the concentration of solar-wind implanted volatiles in lava flows (Fagents et al., 2010).

Although the Lunar Sourcebook (Heiken et al., 1991) and other lunar encyclopedias (Badescu, 2012) contain extensive data on lunar regolith, they focus on understanding the scientific theory behind regolith material properties. Additionally, many critical properties, including specific heat, thermal conductivity, and electrical conductivity are not discussed in detail. These sources present excellent compilations of the theory behind the trends seen in Apollo data, but do not serve as engineering references for accessible functional models of lunar regolith material properties.

* Corresponding author.

E-mail address: schr0910@umn.edu (S.S. Schreiner).

¹ NASA Space Technology Research Fellow, MIT Department of Aeronautics and Astronautics.

² VENCORE-ESC, NASA Kennedy Space Center.

³ Surface Systems Group, ESC-5, NASA Kennedy Space Center.

⁴ Professor of the Practice, MIT Department of Aeronautics and Astronautics.

Here we present models for the density, specific heat, latent heat of melting, thermal conductivity, electrical conductivity, optical absorption length, Gibbs Free Energy, and Enthalpy of Formation of lunar regolith. These models are rooted in data from hundreds of minerals including Apollo samples and analogous materials published in over 25 articles in the literature. The models presented herein describe how regolith material properties depend on temperature, a critical aspect in many thermal-driven engineering applications, especially within the field of ISRU. To allow these property models to be used across a wide range of temperature regimes, the data and fits are not limited to solid granular regolith only, but also extend to the molten (liquid) state. Rumpf et al. (2013) noted that “[regolith] properties have rarely been measured at temperatures greater than 350 K. Thus, the temperature dependencies of regolith properties must be extrapolated from measured values.” By incorporating high-temperature data from lunar regolith simulants, we provide a measure of fidelity for high temperature applications.

Furthermore, the majority of the models presented herein are differentiated based on the type of lunar regolith. That is, separate models are presented for Highlands, High-Ti Mare, and Low-Ti Mare lunar regolith. This allows the models to be tailored to specific lunar applications, while also providing a degree of understanding as to how each material property is affected by regolith composition.

Although regression models are created for each regolith material property, the raw data from the literature survey are also presented in appendices so that additional analysis and data fitting may be performed as necessary.

2. Types of lunar regolith

Lunar regolith can be broadly classified into two categories: Highlands and Mare (Heiken et al., 1991). Highlands regolith is primarily comprised of ancient impact-shocked rock while Mare is comprised of basaltic lava flows in large impact basins (Crawford, 2014). Stoesser et al. (2010) further organized Mare regolith into High-Titanium Mare (≥ 5 wt% TiO_2) and Low-Titanium Mare (< 5 wt% TiO_2) classifications. Due to the differences in geological processes that resulted in Highlands and Mare regolith, the material properties and composition of these two types of regolith differ. This work largely differentiates regolith material properties between Highlands and Mare regolith. Where appropriate, models are further differentiated between High-Ti Mare and Low-Ti Mare regolith.

Lunar regolith is primarily comprised of plagioclase, pyroxene, olivine, and ilmenite, and the concentration of each depends upon location on the lunar surface. Mare regolith contains less plagioclase, but more olivine, pyroxene, and ilmenite (Heiken et al., 1991). Each of these minerals are composed of oxides, including iron(II) oxide (FeO), silica (SiO_2), alumina (Al_2O_3), titania (TiO_2), magnesia (MgO), calcium oxide (CaO), and trace amounts of other minerals and elements. Although the oxides are chemically bound together in various minerals, composition data is often presented in terms of the constituent oxides for simplicity. Oxide composition data from Stoesser et al. (2010) were averaged within each regolith type to generate a single value that represents the expected average oxide composition for each regolith type.

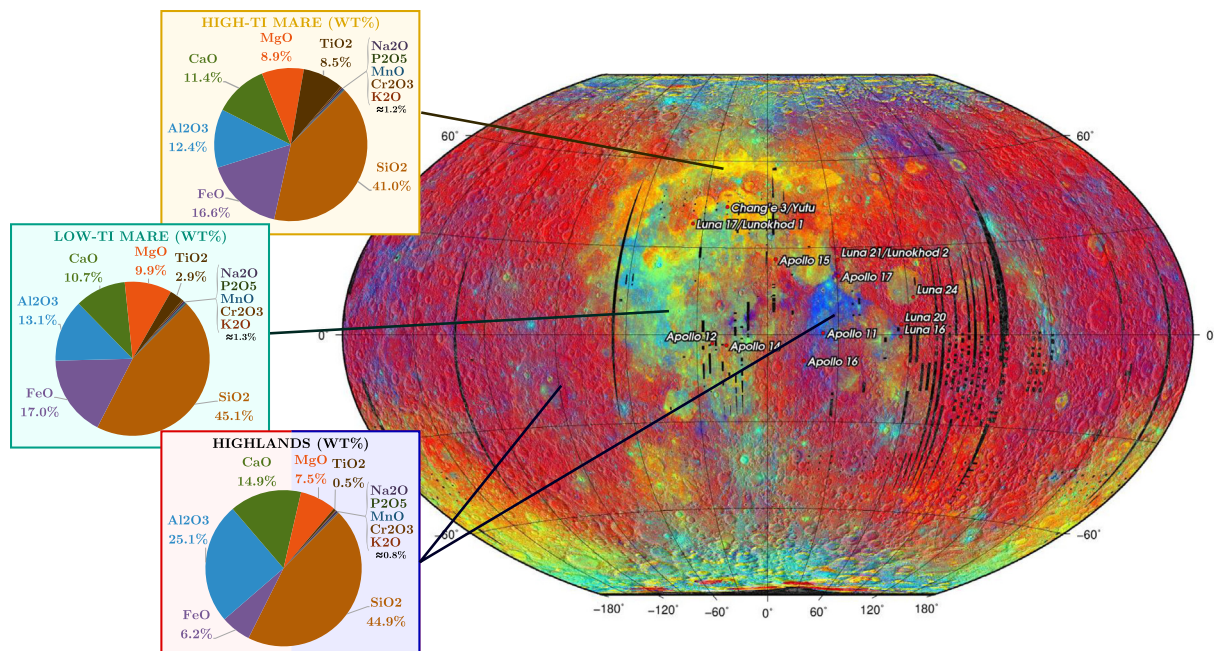


Fig. 1. The composition of three different types of lunar regolith: High-Titanium Mare (yellow), Low-Titanium Mare (cyan), and Highlands (older rock in red, younger rock in blue). Composition data from Apollo and Luna missions (Stoesser et al., 2010) and imagery data from Clementine UVVIS instrument (Lucey et al., 2000). (For interpretation of the references to colour in this figure legend, the reader is referred to the web version of this article.)

Fig. 1 shows the average composition data for each regolith type along with a map of the lunar surface with the lunar High-Ti Mare (yellow), Low-Ti Mare (cyan) and Highlands (older formations in red, younger formations in blue), from the Clementine UVVIS instrument (Lucey et al., 2000). As can be seen in Fig. 1, Highlands regolith dominates the lunar surface, covering 84% of the lunar nearside and 99% of the lunar farside (Heiken et al., 1991). The averaged composition data are also presented in Table A.7.

3. Density

The bulk density of lunar regolith plays a large role in many engineering applications, as it drives the relationship between regolith mass and volume. This relationship is critical in sizing hardware elements such as regolith hoppers, reactors, and excavators. Additionally, density affects the modeling of lunar geological processes (Fagents et al., 2010).

The density of granular lunar regolith depends upon depth and compaction, but an average value of 1500 kg/m³ appears to be appropriate for the top 15 cm of lunar soil, based on data from the Apollo and Luna missions (Heiken et al., 1991). Naturally, the expected density will rise with depth and compaction, though this value appears to be bounded below 1790 kg/m³ for soil as deep as 60 cm (Heiken et al., 1991). The appropriate density should be selected from within this range based on the expected compaction in a particular application.

For molten lunar regolith, the density varies with both temperature and composition. The model from Stebbins et al. (1984) for the volume of molten silicates was algebraically manipulated to create a density model. This model contains a dependence on both composition and temperature, allowing it to differentiate based on the compositions presented in Section 2. The model, shown in Eq. (1), was used for the density of each of the three types of molten lunar regolith:

$$\rho = \frac{r_1}{r_2 + r_3(T - 1873)}, \quad (1)$$

where ρ is the density (kg/m³), T is the temperature (K), and r_i are regression coefficients, shown in Table 1. The regression coefficients were calculated by weighting the oxide-specific coefficients by the oxide molar fraction for each type of regolith. The oxide-specific coefficients are derived from a linear regression of data from several dozen

Table 1
The coefficients for the Stebbins density model (Eq. (1)) applied to three types of lunar regolith.

	r_1	r_2	r_3
Highlands	6.345×10^4	24.11	0.001206
High-Ti Mare	6.333×10^4	22.48	0.001982
Low-Ti Mare	6.384×10^4	23.01	0.001612

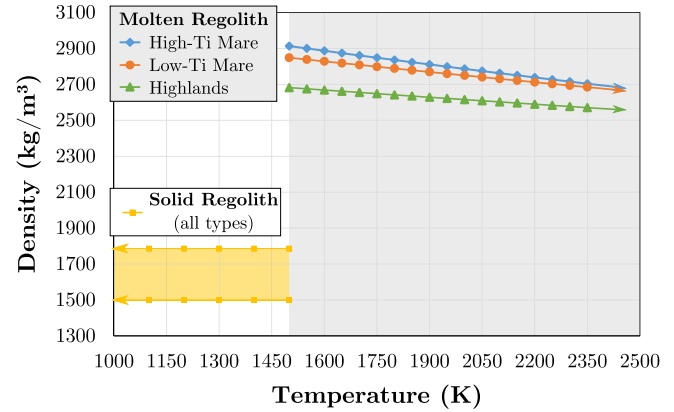


Fig. 2. The variation of lunar regolith density with temperature. The density of solid regolith (for all types) is taken from Heiken et al. (1991) and the density molten lunar regolith (differentiated or High-Ti Mare, Low-Ti Mare and Highlands) is calculated using the density model from Stebbins et al. (1984).

molten silicates between 1673 K and 1873 K (Stebbins et al., 1984).

The predictions from the density model are shown in Fig. 2 for all three types of lunar regolith. The Mare regolith variants have a higher predicted density than the Highlands, due to the relatively larger concentration of TiO₂ in Mare regolith compared to the relatively larger concentration of Al₂O₃ in Highlands regolith (see Fig. 1). The relatively higher density for Mare regolith compared to anorthite-rich Highlands also aligns with the trends from Arndt et al. (1979). The values predicted by the model compare well with the range of 2490–2890 kg/m³ measured for molten JSC-1A lunar simulant (Kallerud et al., 2011). Furthermore, the general decrease in density with temperature agrees well with the trends for melts with significant amounts of SiO₂, CaO, MgO, FeO, and Al₂O₃ (Allibert et al., 1995).

4. Specific heat

Many regolith processing systems require heating regolith from ambient to significantly higher temperatures (Taylor and Carrier, 1992). To accurately predict the power requirements for regolith heating, the specific heat over the relevant temperature range must be well known.

For temperatures below 350 K, a fourth-order polynomial fit of data from samples Apollo 14, 15, and 16 (Hemingway et al., 1973) was used:

$$C_p = c_a + c_b T + c_c T^2 + c_d T^3 + c_e T^4, \quad (2)$$

where C_p is the specific heat (in J/(kg·K)), T is the temperature (in K), and c_a, c_b, c_c, c_d , and c_e are regression coefficients from Hemingway et al. (1973), shown in Table 2.

For solid regolith above 350 K, a model for silicate minerals from Stebbins et al. (1984) was employed to predict the heat capacity:

Table 2

The coefficients for the specific heat of lunar regolith model between 100 K and 350 K from Hemingway et al. (1973).

c_a	-2.32×10^{-2}	c_d	-7.37×10^{-8}
c_b	2.13×10^{-3}	c_e	9.66×10^{-11}
c_c	1.50×10^{-5}		

$$C_p = \sum_i \chi_i c_{f,i} + T \sum_i \chi_i c_{g,i} + T^{-2} \sum_i \chi_i c_{h,i}, \quad (3)$$

where χ_i is the mole fraction of oxide specie i in lunar regolith, and $c_{f,i}$, $c_{g,i}$, and $c_{h,i}$ are coefficients derived from linear regression of data from several dozen minerals (Stebbins et al., 1984). Table 3 shows the resultant coefficients, calculated by weighting the oxide-specific coefficients by molar fraction.

For molten regolith, the specific heat remains relatively constant with temperature but varies with composition, as predicted by Stebbins et al. (1984):

$$C_p = \sum_i \chi_i C_{l,i}, \quad (4)$$

Table 3

The coefficients for the Stebbins heat capacity model (Eqs. (3)), in which oxide-specific coefficients are weighted by molar fraction. The summation represents a summation over all oxide species in lunar regolith.

	$\sum_i \chi_i c_{f,i}$	$\sum_i \chi_i c_{g,i}$
High-Ti Mare	8.820×10^2	3.083×10^{-1}
Low-Ti Mare	9.093×10^2	2.870×10^{-1}
Highlands	9.530×10^2	2.524×10^{-1}
	$\sum_i \chi_i c_{h,i}$	$\sum_i \chi_i C_{l,i}$
High-Ti Mare	-2.278×10^7	1.531×10^3
Low-Ti Mare	-2.469×10^7	1.539×10^3
Highlands	-2.645×10^7	1.565×10^3

where $C_{l,i}$ is the coefficient of oxide specie i in lunar regolith, formed from a linear regression of a database of 58 different compositions (Stebbins et al., 1984). The resultant weighted coefficients are also shown in Table 3.

The piecewise specific heat model from Eqs. (2)–(4) are shown together in Fig. 3. The data from Hemingway et al. (1973), also given in Table A.8, show little variation between Apollo missions, as seen in the bottom right of Fig. 3. The model from Stebbins et al. (1984) compares reasonably well with the Apollo data near 350 K. The specific heat increases by an average of 248 J/kg-K at the melting temperature (1500 K), which compares quite well with the value of 243 J/kg-K observed across a wide range of minerals by Arndt et al. (1979). The predictions for molten lunar regolith are in the range of 1460–1700 J/kg-K cited by Fagents et al. (2010). The data in Fig. 3 fall between the curves from Colozza (1991) and lunar simulant FJS-1, fabricated by the Japanese Aerospace Agency (Wakabayashi and Matsumoto, 2006). Data on the specific heat of FJS-1 are also shown in Table A.9.

5. Latent heat of melting

The latent heat of melting (also known as latent heat of fusion) is a critical parameter in modeling systems that interact with regolith across the phase transition between the solid and molten states (Solomon et al., 1992; Schreiner et al., 2015). Additionally, the latent heat of melting plays a significant role in modeling the cooling of lunar lava flows (Rumpf et al., 2013).

The latent heat of melting naturally depends on regolith composition and therefore regolith type. The modal

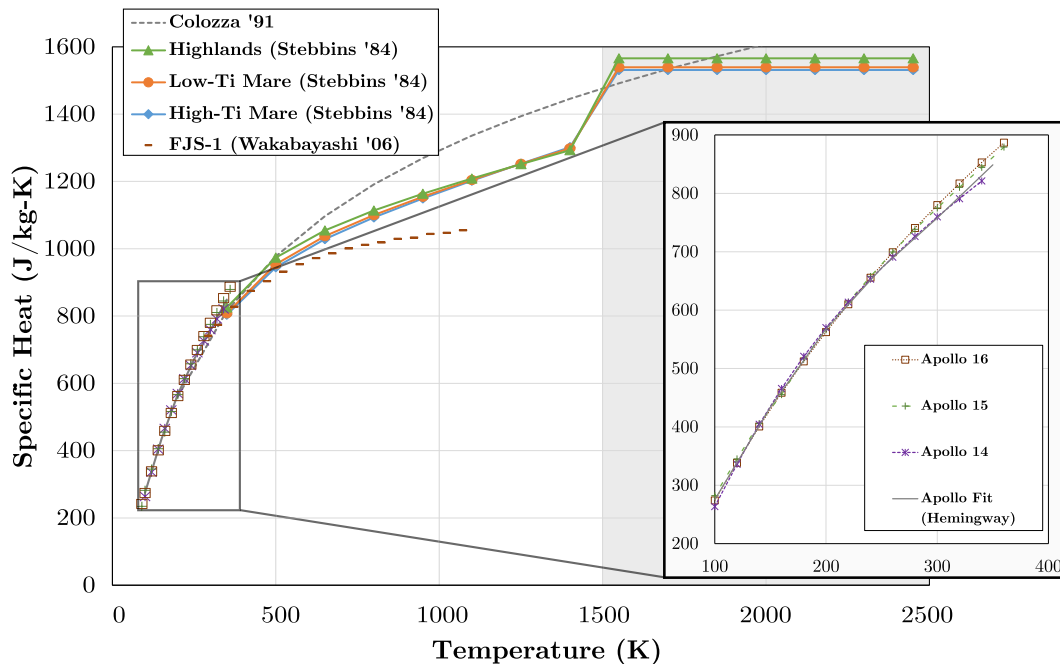


Fig. 3. The specific heat model for lunar regolith. In the lower temperature regime (≤ 350 K), a fit based on Apollo data from Hemingway et al. (1973) is used. At higher temperatures (> 350 K), a model by Stebbins et al. (1984) is used.

Table 4

The latent heat (L_{heat}) of melting for High-Ti Mare (HTM), Low-Ti Mare (LTM), and Highlands (HLD) regolith, calculated by weighting the latent heat of melting for the constituent minerals from [Richet and Bottinga \(1986\)](#) by the molar fraction from [Basu and Riegsecker \(2000\)](#).

	Molar fraction (χ_i)			Mineral L_{heat} ($\frac{\text{kJ}}{\text{mol}}$)
	HTM	LTM	HLD	
Plagioclase	0.2830	0.2875	0.7320	134.3
Olivine	0.0465	0.0880	0.0230	83.2
Pyroxene	0.5945	0.5890	0.2440	65.1
Ilmenite	0.0760	0.0355	0.0010	21.7
Regolith L_{heat} ($\frac{\text{kJ}}{\text{kg}}$)	449.2	457.7	478.6	

mineralogical distribution of plagioclase, olivine, pyroxene, and ilmenite from [Basu and Riegsecker \(2000\)](#) is presented in [Table 4](#) along with the latent heat of melting for each mineral from [Richet and Bottinga \(1986\)](#). To calculate the latent heat of melting for each regolith type, the latent heat of melting for each mineral was weighted by molar fraction, the results of which are shown in bold in the bottom row of [Table 4](#).

As shown in [Table 4](#), the latent heat of melting for lunar regolith is in the range 450–480 kJ/kg, depending on regolith type. These values are slightly below the reported range of 476–506 kJ/kg for similar minerals analyzed by [Kojitani and Akaogi \(1995\)](#), likely due to differences in composition. Conversely, these predictions are higher than the value derived from [Colozza \(1991\)](#) of 400 kJ/kg (calculated by integrating the value of 1.429 kJ/kg-K over the melting range of 1373–1653 K). [Fagents et al. \(2010\)](#) also notes that values near 500–600 kJ/kg seem appropriate for basaltic compositions similar to lunar regolith. It is worth noting that the values reported here are significantly higher than the value reported for lunar simulant MLS-1 of 161.2 kJ/kg ([Richter, 1992](#)), although this value is for a sample size of 33.2 mg and the uncertainty on this value is unknown.

6. Thermal conductivity

The thermal conductivity of lunar regolith naturally plays a large role in modeling thermal transport. Thermal conductivity affects the expected thermal performance of regolith processing reactors, and double-walled hoppers and augers intended to act as heat exchangers ([Linne, 2010](#)). The thermal conductivity also affects simulations of lunar geological evolution ([Fagents et al., 2010](#)) as well as interpretations of lunar surface brightness ([Keihm and Langseth, 1973](#)).

For the thermal conductivity of solid lunar regolith, data from the FJS-1 lunar simulant ([Wakabayashi and Matsumoto, 2006](#)) and Apollo samples ([Langseth et al., 1972](#); [Cremers, 1975](#)) were used. Data for FJS-1 are an order of magnitude higher than most of the Apollo data. It is possible that the FJS-1 data come from experiments with an overhead atmosphere or significant regolith compaction (it is not specified in the report), which has been

shown to increase the thermal conductivity of granular materials by an order of magnitude ([Horai, 1981](#)). The data from the Apollo 15 in situ drilling experiment ([Langseth et al., 1972](#)) are also higher than that of the other Apollo experiments. This is likely due to the fact that the thermal conductivity of the top loose layer is significantly lower than that of the compacted lower regolith below 2 cm ([Heiken et al., 1991](#)). For a given application, the appropriate value for the thermal conductivity of granular lunar regolith must be chosen based on the expected compaction of the regolith.

Thermal conductivity data were unavailable for molten lunar regolith, so a set of similar minerals were selected from [Allibert et al. \(1995\)](#), [Snyder et al. \(1994\)](#), and [Kang and Morita \(2006a\)](#). These selected species were representative of the large concentrations of SiO_2 , CaO , Al_2O_3 , MgO and FeO (more commonly Fe_2O_3 in terrestrial minerals) present in lunar regolith.

The combined data for solid and molten lunar regolith are presented in [Fig. 4](#) and shown in [Tables A.10, A.11, A.12, and A.13](#). Note that the Apollo data in the figure are from regression fits of the sample data. The thermal conductivity for solid, granular regolith rises with temperature because granular, porous materials in vacuum will have two primary heat transfer mechanisms. The first is solid conduction through the particles and their contact surfaces, and the second is radiation in the inter-granular cavities. [Watson \(1964\)](#) first modeled this phenomenon using a constant for the conduction term with a third-order dependence on temperature to approximate complex emission-absorption radiative mechanism. This model has been used in the vast majority of work on the thermal conductivity of solid granular lunar regolith ([Langseth et al., 1972](#); [Cremers, 1975](#)) and was fit to the solid data (adjusted $R^2 = 0.86$, RMSE = 0.0090 W/m-K):

$$k = 0.001561 + 5.426 \times 10^{-11} (T^3), \quad (5)$$

where k is the thermal conductivity (W/m-K) and T is the temperature (K).

As seen in the right of [Fig. 4](#), the data for molten silicates similar to lunar regolith exhibit a decrease in thermal conductivity with temperature. Following the example of [Kang and Morita \(2006\)](#), the equation below was fit to the molten data (adjusted $R^2 = 0.67$, RMSE = 0.43 W/m-K):

$$k = \exp \left(-9.332 + \frac{1.409 \times 10^4}{T} \right). \quad (6)$$

The low R^2 value is due to the wide spread in the data due to composition. Future work can address differentiating the molten thermal conductivity model based on regolith composition.

As shown in [Fig. 4](#), the piece-wise model from [Eq. \(5\)](#) and [\(6\)](#) exhibits a clear discontinuity at the melting temperature (1500 K). In reality, portions of regolith will exist in the molten and solid states in the vicinity of the melting temperature, smoothing out this discontinuity. Furthermore, piecewise functions often impede the convergence of simulations in which the phase transition must be

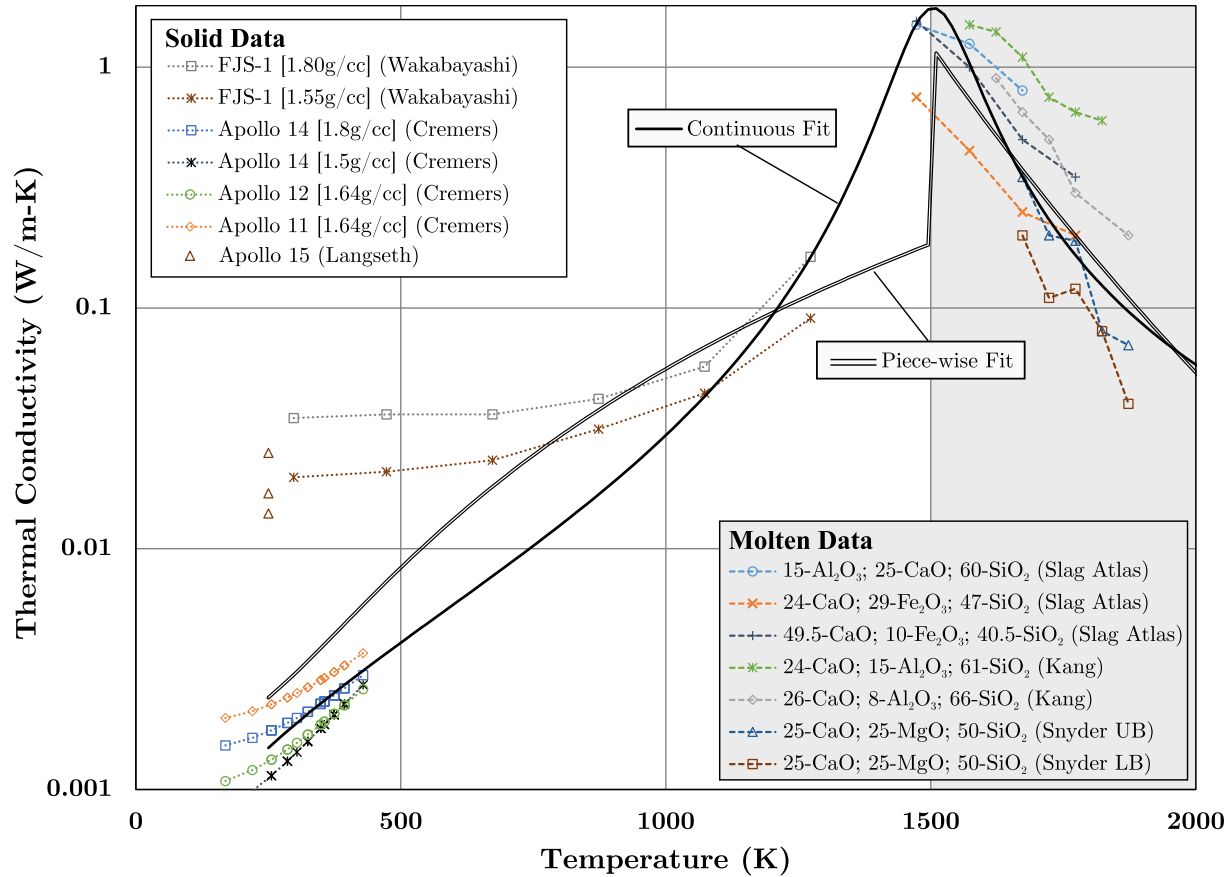


Fig. 4. The thermal conductivity from Apollo surface experiments, the FJS-1 simulant (Wakabayashi and Matsumoto, 2006) and liquid silicates similar to lunar regolith (Allibert et al., 1995; Snyder et al., 1994).

modeled (Schreiner et al., 2015). To this end, an empirical continuous model was fit over both the solid and molten data, for use in simulations that require rapid convergence (adjusted $R^2 = 0.96$, RMSE = 0.096 W/m-K):

$$k = \frac{0.01257(T') + 0.0172}{(T')^2 - 2.874(T') + 2.085}, \quad (7)$$

where T' is the temperature in K normalized by a mean 691.7 and standard deviation 564.3. Fig. 4 shows the continuous and piece-wise models for the thermal conductivity of lunar regolith. Overall, the trends observed in the continuous regression fit are in agreement with those observed in the range of minerals from Allibert et al. (1995).

The appropriate model, whether continuous or piece-wise, must be chosen based upon application. Furthermore, Fig. 4 demonstrates how the degree of compaction plays a large role in the thermal conductivity of granular lunar regolith at low temperatures. For a given application, the appropriate low temperature data should be selected based upon the expected compaction.

7. Electrical conductivity

The electrical conductivity of lunar regolith affects performance predictions for electrochemical reactors

(Schreiner et al., 2015) and plays a role in simulating geophysical aspects of the lunar interior (Olhoeft et al., 1974).

For solid lunar regolith, the electrical conductivity is expected to be close to zero. Electrical conductivity data from Apollo samples 12002,85 and 65015,6 (Olhoeft et al., 1974) was utilized. For molten lunar regolith, data was taken from a lunar regolith analog with a composition of 25% CaO, 25% MgO, and 50% SiO₂ with varying amounts of FeO added (Ducret et al., 2002). The mixture with 5 wt% FeO added was used to approximate both Mare types of regolith and data for the melt with 15 wt% FeO added was used for the Highlands, to match the compositions shown in Fig. 1. Additional data on iron-rich basalt from Carroll (1983) was used for Mare regolith. Fig. 5 shows the electrical conductivity data combined from all of these sources, which is also presented in Table A.14.

Intuitively, solid granular lunar regolith has a much lower electrical conductivity than the molten state. Starting around the glass transition temperature, which is around 2/3 of the melting temperature (Vila et al., 2006) or 1000 K, the electrical conductivity begins to rise noticeable above zero. This can be attributed to the increase in relaxation and transport mechanisms (Vila et al., 2006) and, at higher temperatures, the gradual transition from the solid

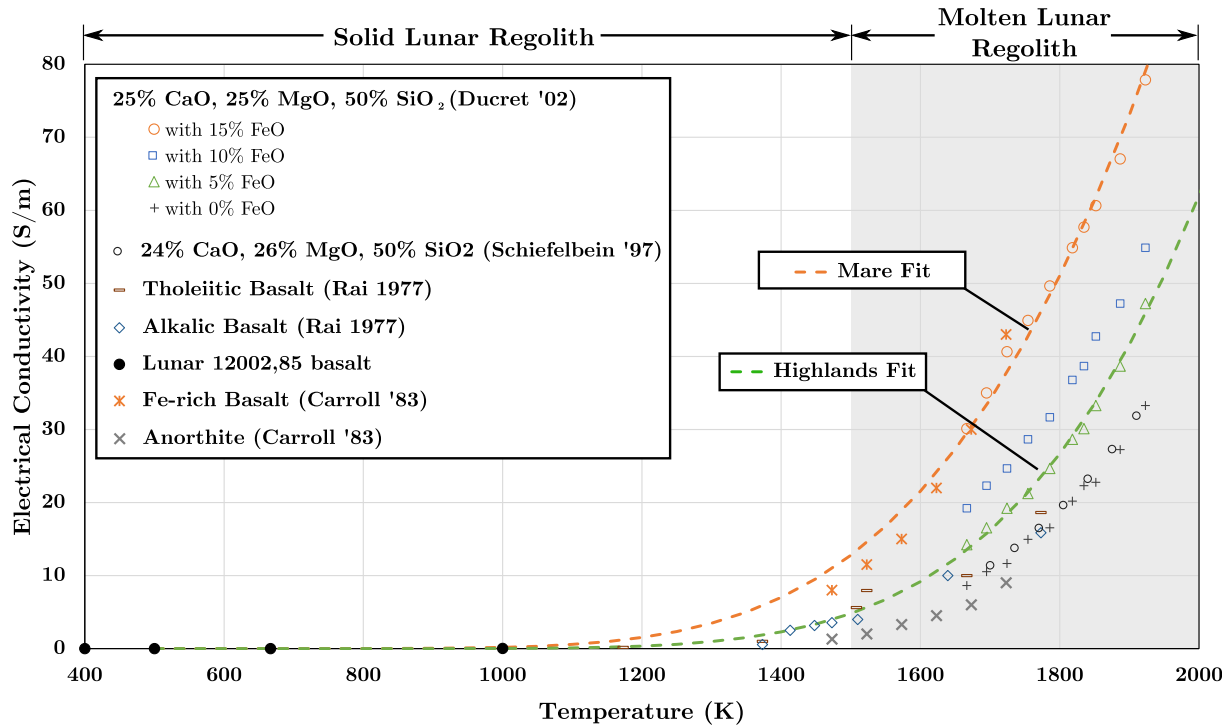


Fig. 5. Data of electrical conductivity for lunar regolith and similar materials. A fit is overlaid for compositions similar to Highlands and Mare lunar regolith. The electrical conductivity begins increasing around the melting temperature due to increased ionic conductivity via a decrease in viscosity at higher temperatures.

Table 5

The regression coefficients for the model of electrical conductivity of lunar regolith (Eq. (8)), differentiated for Mare and Highlands regolith.

	Mare	Highlands
e_a	3.130×10^4	1.291×10^5
e_b	1.154×10^4	1.528×10^4

to molten state. The increase in electrical conductivity past the melting point is due to the decrease in viscosity and subsequent rise in ionic mobility (Colson and Haskin, 1990), which is a primary driver of electrical conductivity in molten oxides (Schiefelbein and Sadoway, 1997).

The electrical conductivity data for both solid and molten regolith was fit with a Vogel–Tamman–Fulcher (VTF) equation (Vogel, 1925; Tamman and Heese, 1926; Fulcher, 1925), as it has been shown to match the temperature dependence of the electrical conductivity of ionic liquids quite well (Vila et al., 2006):

$$\sigma_e = e_a \exp\left(\frac{-e_b}{T - T_g}\right), \quad (8)$$

where σ_e is the electrical conductivity (in S/m), T is the temperature (in K), T_g is the glass transition temperature (often fit with regression analysis), and e_a and e_b are regression coefficients presented in Table 5 (adjusted $R^2 = 0.997$). Note that T_g had to be set to zero to avoid vertical asymptotes in the low temperature regime.

As observed in Fig. 5, the model compares reasonably well with data for Tholeiitic and Alkali basalts (Rai, 1977), data on basalt and anorthite (Carroll, 1983), and data from Schiefelbein and Sadoway (1997). Clearly the electrical conductivity increases with FeO concentration, due to increased electronic conductivity of iron oxides (Sirk et al., 2010). In the context of lunar regolith, this means that one can expect a higher electrical conductivity for Mare regolith compared to Highlands.

Although a continuous fit over the solid and molten data enables rapid physical simulation across the phase boundary (Schreiner et al., 2015), this could possibly introduce some reduction in model fidelity (the VTF fit in Eq. 8 is intended for ionic liquids rather than solids). To this end, regression fits of the data above 1500 K were compared to the regression fits for the full temperature range. Average discrepancies under 1% were observed between the two fits in the range of 1500–2000 K for both Highlands and Mare data, indicating that the full data regression fit can function well in the high temperature regime. For applications in which the electrical conductivity of solid regolith at low temperatures is of critical importance, the fit given by Eq. (8) may not be appropriate. The reader is directed to the work of Olhoeft et al. (1974), which addresses the hysteresis observed in low temperature data and provides exponential fits of data from two Apollo samples. For applications in which the low temperature data must simply be significantly lower than the high temperature data (Schreiner et al., 2015), the model in Eq. (8) is adequate.

8. Optical absorption length

For sintering and molten regolith processing, the optical absorption length affects radiative thermal transport through the semi-translucent medium (Sibille and Dominguez, 2012; Balasubramaniam et al., 2010). Wavelength-dependent data on molten glasses from Sibille and Dominguez (2012) was first fit with a step function of 0.3 cm^{-1} for wavelengths below 2750 nm and 4 cm^{-1} above 2750 nm. The upper value of the step function compares well with those of Arndt et al. (1979) for basalt and anorthosite samples at higher wavelengths, but the drop to lower absorption lengths at lower wavelengths remains to be validated. This step function was then weighted by the Planck black body energy density and integrated over all wavelengths to determine the average absorption length at a given temperature ($\alpha(T)$):

$$\alpha(T) = \frac{\int_0^\infty P(\lambda, T) \alpha(\lambda) d\lambda}{\int_0^\infty P(\lambda, T) d\lambda}, \quad (9)$$

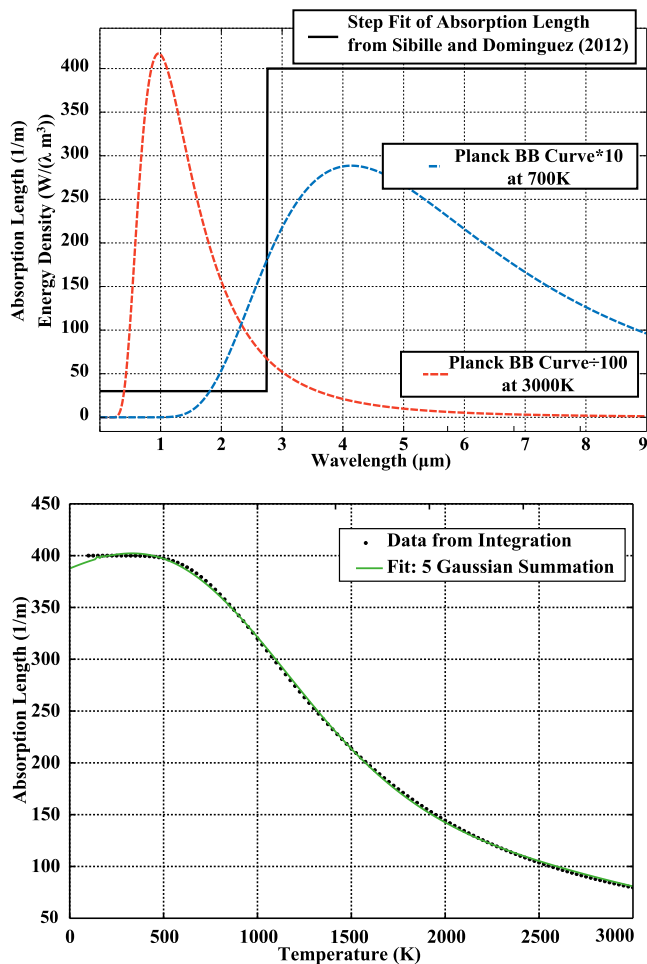


Fig. 6. (left) Absorption length data from Sibille and Dominguez (2012) fit with a step function (black solid line) overlaid with the Planck black body spectral energy density at two different temperatures (dashed lines). (right) The wavelength-dependent step function was integrated over the Planck curve to calculate the average absorption length as a function of temperature.

Table 6

The coefficients for the optical absorption length model (Eq. (11)), which sums five Gaussian functions together.

	Gauss-1	G-2	G-3	G-4	G-5
a_i	465	−0.650	163	0.325	1.45
b_i	−3670	200	528	175	150
c_i	5040	4.69	905	4.40	3.54

where $\alpha(\lambda)$ is the absorption coefficient as a function of wavelength, λ , and $P(\lambda)$ is the spectral energy density as a function of wavelength from Planck's Law (Planck, 1914):

$$P(\lambda, T) = \frac{8\pi hc^2}{\lambda^5} \left(\frac{1}{\exp\left(\frac{hc}{k_B T \lambda}\right) - 1} \right), \quad (10)$$

where h is Planck's constant, c is the speed of light, and k_B is Boltzmann's constant.

The left plot in Fig. 6 shows the step function for absorption length derived from Sibille and Dominguez (2012) (black solid line) overlaid with the Planck black body spectral energy density curve at two different temperatures, 700 K (blue) and 3000 K (red). The right plot in Fig. 6 shows the resultant absorption length as a function of temperature ($\alpha(T)$ from Eq. (9)) with a regression fit using a summation of five Gaussian functions:

$$\alpha(T) \approx a_1 e^{-\left(\frac{T-b_1}{c_1}\right)^2} + \dots + a_5 e^{-\left(\frac{T-b_5}{c_5}\right)^2} \quad (11)$$

where a_i , b_i , and c_i are regression coefficients shown in Table 6 (adjusted $R^2 = 0.999$).

The trends in the right-hand plot in Fig. 6 reveal that the absorption length decreases at higher temperatures. The model presented here is based on absorption length data from molten glasses and the uncertainty concerning the absorption length of actual lunar regolith warrants further examination. Arndt et al. (1979) observed that basaltic droplets were essentially opaque while anorthositic droplets were semi-transparent. Future work can address differentiating the absorption length model based on regolith type and validating the high temperature absorption behavior.

9. Gibbs Free Energy & Enthalpy of Formation

The Gibbs Free Energy (ΔG) and Enthalpy of Formation (ΔH) for the oxide species in lunar regolith describe the energy required to break the chemical bonds, a critical step in many regolith processing techniques, including Molten Regolith Electrolysis and Pyrolysis (Taylor and Carrier, 1992). Data for these two values for each oxide specie in lunar regolith was obtained from the NIST-JANAF thermochemical tables (Chase, 1998). Due to the fact that ΔG and ΔH often change with phase, the data was separated into high temperature and low temperature data and fit with the following equations (Chase, 1998):

$$\Delta G(T) = a_G + b_G T \log_{10}(T) + c_G T, \quad (12)$$

$$\Delta H(T) = a_H + b_H T, \quad (13)$$

where T is the temperature (K) and a_G, b_G, c_G, a_H , and b_H are regression coefficients for each oxide specie, shown in Table A.15. There is good agreement between the two intercepts (a_G and a_H), as one would expect.

Fig. 7 shows the low temperature (solid lines) and high temperature (dashed lines) fits compared to the data. As one would expect, the Gibbs Free Energy rises significantly with temperature, while the Enthalpy of Formation remains relatively constant across a wide temperature

range. The Enthalpy of Formation data indicates that iron oxide (FeO) is the most attractive oxide specie for oxygen production from a chemical perspective, as it requires the least amount of energy to isothermally reduce to its base metal and oxygen. Titania (TiO_2) and silica (SiO_2) are the next most attractive targets, requiring slightly less than twice the energy of iron oxide. Alumina (Al_2O_3), magnesia (MgO), and calcium oxide (CaO) present the least chemically attractive objects for reduction.

Although the source data for Gibbs Free Energy and Enthalpy of Formation is rooted in significant experimental work (Chase, 1998), the values may need to be adjusted

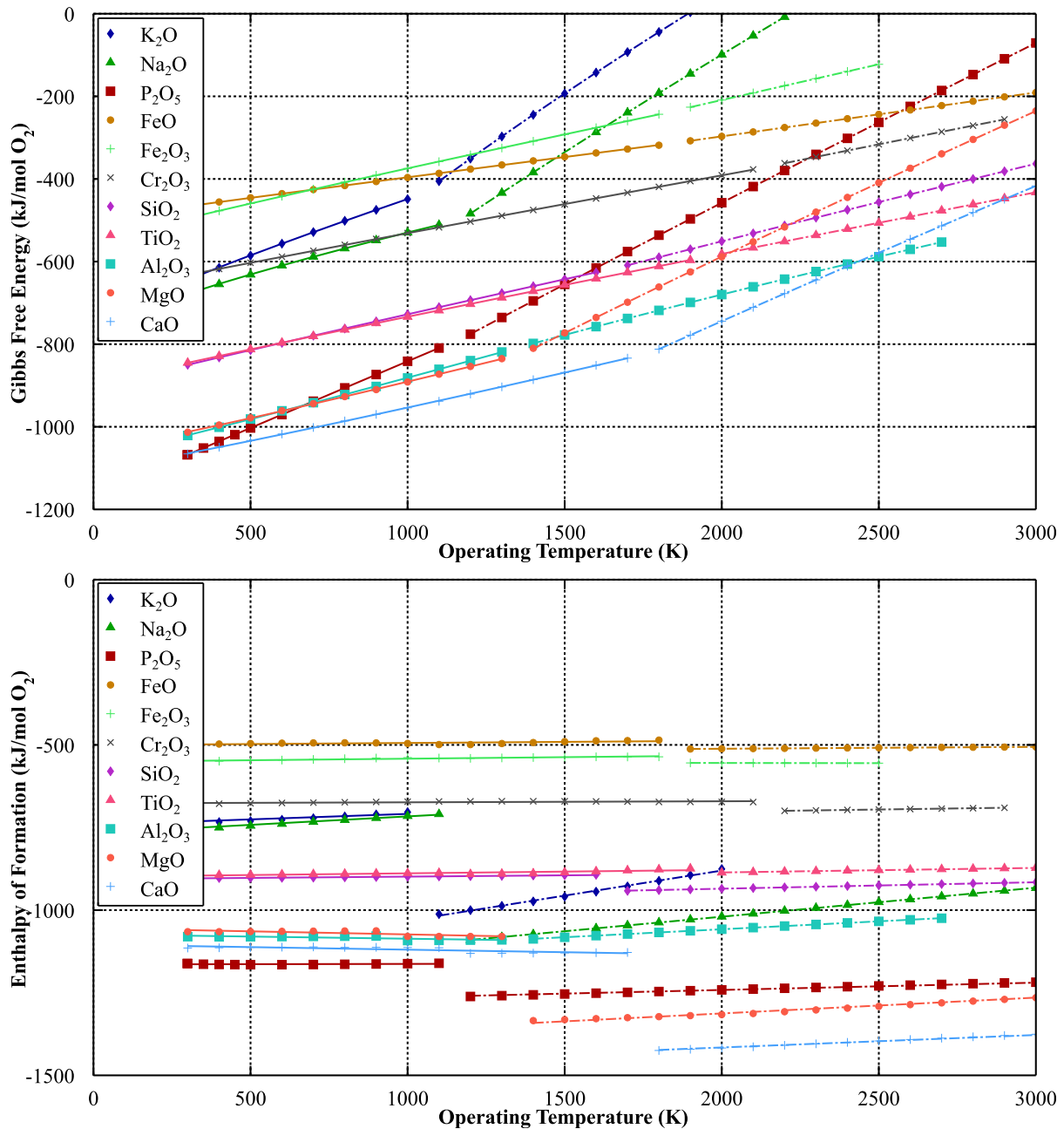


Fig. 7. The Gibbs Free Energy (top) and Enthalpy of Formation (bottom) for each oxide specie in lunar regolith (Chase, 1998), with linear fits over the high temperature data.

with activity coefficients based on the relative concentration of each oxide, though the effect is not anticipated to significantly change these values.

10. Conclusions

In this work we present several models for the material properties of Highlands and Mare lunar regolith, including chemical composition, density, specific heat, latent heat of melting/fusion, thermal conductivity, electrical conductivity, optical absorption length, Gibbs Free Energy and the Enthalpy of Formation. The models incorporate data from hundreds of minerals, including Apollo and Luna samples as well as a vast array of lunar regolith simulants.

The data used to build the property models spans a wide temperature range (≈ 100 K to 2000 K), including both the solid and molten (liquid) states. By including high temperature lunar simulant data, the models extend previous work significantly beyond the traditional range of 100–350 K (Rumpf et al., 2013) and increase our understanding of the high-temperature behavior of lunar regolith.

It is found that the density of molten lunar regolith varies significantly with temperature and regolith type (Highlands or Mare). The specific heat is within 5% for Highlands and Mare regolith, but varies significantly with temperature. The latent heat of melting is slightly higher ($\approx 7\%$) for Highlands regolith due to the increased amount of plagioclase. The thermal conductivity varies widely depending upon the density, compaction, and temperature of regolith, though the effect of regolith composition/type is still uncertain. Electrical conductivity rises with temperature and is higher for Mare regolith due to the higher concentration of iron oxide. The optical absorption length data are preliminary at best, but indicates that in molten regolith radiation may travel on the order of a few millimeters before being reabsorbed and scattered.

Future work can address the behavior of lunar regolith near the glass transition temperature circa 1000 K. Data on the optical absorption length are particularly sparse for lunar regolith. Electrical and thermal conductivity at high temperatures are also somewhat uncertain. The effect of compaction on many properties, including thermal conductivity and density, also remains an avenue of future work.

The regolith material property models presented herein can be used to inform the design and analysis of regolith processing hardware, such as excavators, ISRU reactors, and regolith transport devices. Furthermore, these models can also be leveraged to better inform simulation of lunar geological processes. By integrating data from hundreds of minerals in over 25 articles in the literature, this work provides a unified source of thermophysical property models for lunar regolith that can benefit future analysis.

Acknowledgments

This work was supported by a NASA Space Technology Research Fellowship (Grant #NNX13AL76H). Any

opinions, findings, and conclusions or recommendations expressed in this material are those of the author and do not necessarily reflect the views of NASA.

Appendix A. Data Tables

Table A.7

The weight percent and mole percent chemical compositions of lunar regolith, categorized in High-Ti Mare (HTM), Low-Ti Mare (LTM), and Highlands (HL).

Oxide specie	Weight percent			Mole percent		
	HTM	LTM	HL	HTM	LTM	HL
K ₂ O	0.2	0.1	0.8	0.2	0.2	0.1
Na ₂ O	0.4	0.4	2.8	0.4	0.4	0.4
P ₂ O ₅	0.2	0.1	0.7	0.2	0.4	0.2
FeO	17.2	6.3	3.5	17.8	18.4	6.4
Cr ₂ O ₃	0.4	0.1	0.0	0.9	0.9	0.3
MnO	0.2	0.1	0.2	0.2	0.2	0.1
SiO ₂	45.4	45.0	47.5	36.7	40.8	38.8
TiO ₂	2.9	0.5	1.5	10.2	3.5	0.6
Al ₂ O ₃	13.2	25.1	15.0	18.8	20.1	36.7
MgO	10.0	7.6	9.0	5.3	6.0	4.4
CaO	10.8	14.9	10.5	9.5	9.0	12.0

Table A.8

Specific Heat data for lunar regolith from Apollo samples as reported by Hemingway et al. (1973).

Temp. (K)	Specific heat (J/kg-K) by Lunar sample number				
	14321,153	14163,186	15555,159	15301,20	60601,31
90			228.9	240.6	241.8
100	253.6	273.6	292.0	272.4	274.1
120	322.6	349.4	354.8	335.6	338.5
140	395.0	413.8	415.1	396.6	400.8
160	459.0	472.4	472.0	438.5	458.6
180	512.1	529.7	525.5	507.1	512.1
200	558.6	581.2	575.7	557.3	562.3
220	602.1	625.1	623.0	604.6	610.0
240	643.5	662.7	666.9	648.9	655.6
260	681.2	700.4	708.4	690.8	699.1
280	715.0	737.6	746.8	730.1	740.6
300	748.5	771.1	782.8	767.3	779.9
320	783.2	798.7	817.1	803.7	817.1
340	817.1	825.5	850.2	838.9	853.1
360			886.2	872.4	887.0

Table A.9

Data on the specific heat of lunar simulant FJS-1 (Wakabayashi and Matsumoto, 2006).

Temp. (K)	Sp. Heat (J/kg-K)	Temp. (K)	Sp. Heat (J/kg-K)	Temp. (K)	Sp. Heat (J/kg-K)
293	741.6	573	954.0	873	1029.6
323	774.0	623	972.0	923	1033.2
373	828.0	673	986.4	973	1044.0
423	874.8	723	1000.8	1023	1047.6
473	903.6	773	1011.6	1073	1054.8
523	932.4	823	1018.8		

Table A.10

(top rows) Thermal conductivity (k) data from Apollo 12 samples (Cremers, 1975) over a range of temperature (T). (bottom row) Thermal conductivity data from the Apollo 15 drilling experiment as a function of depth (D) at an estimated temperature of 250 K (Langseth et al., 1972).

T (K)	k ($\frac{W}{m \cdot K}$)	T (K)	k ($\frac{W}{m \cdot K}$)	T (K)	k ($\frac{W}{m \cdot K}$)
169	0.00114	325	0.00219	374	0.00270
256	0.00121	349	0.00241	374	0.00278
256	0.00129	349	0.00243	374	0.00283
286	0.00161	349	0.00246	393	0.00259
286	0.00161	356	0.00197	394	0.00268
304	0.00207	356	0.00205	429	0.00339
324	0.00180				
D (m)	k ($\frac{W}{m \cdot K}$)	D (m)	k ($\frac{W}{m \cdot K}$)	D (m)	k ($\frac{W}{m \cdot K}$)
0.49	0.014	0.91	0.017	1.38	0.025

Table A.11

Regression fit coefficients from Cremers (1975) for Eq. (5) for data from several Apollo samples and terrestrial basalt with a range of densities (ρ).

	Apollo 11	Apollo 14	Apollo 14	Apollo 12
ρ ($\frac{g}{cm^3}$)	1.64	1.50	1.80	1.64
k_A ($\frac{W}{m \cdot K}$)	1.87×10^{-3}	7.16×10^{-4}	1.43×10^{-3}	9.85×10^{-4}
k_B ($\frac{W}{m \cdot K^4}$)	2.3×10^{-11}	2.54×10^{-11}	1.97×10^{-11}	2.06×10^{-11}

Table A.12

Thermal conductivity data for lunar simulant FJS-1 with three different densities (Wakabayashi and Matsumoto, 2006).

Temp. (K)	Thermal conductivity (W/m-K)		
	1.55 g/cm ³	1.65 g/cm ³	1.80 g/cm ³
298	1.98×10^{-2}	2.33×10^{-2}	3.49×10^{-2}
473	2.09×10^{-2}	2.44×10^{-2}	3.61×10^{-2}
673	2.33×10^{-2}	2.56×10^{-2}	3.61×10^{-2}
873	3.14×10^{-2}	3.49×10^{-2}	4.19×10^{-2}
1073	4.42×10^{-2}	5.23×10^{-2}	5.70×10^{-2}
1273	9.07×10^{-2}	1.14×10^{-1}	1.63×10^{-1}

Table A.13

Data on the thermal conductivity (W/m-K) for molten regolith analogs from various sources.

Kang and Morita (2006)			Snyder et al. (1994) (25-CaO; 25-MgO; 50-SiO ₂)		
Temp. (K)	24-CaO; 15-Al ₂ O ₃ ; 61-SiO ₂	26-CaO; 8-Al ₂ O ₃ ; 66-SiO ₂	Temp. (K)	Upper bound	Lower bound
1573	1.5		1673	0.35	0.2
1623	1.4	0.9	1723	0.2	0.11
1673	1.1	0.65	1773	0.19	0.12
1723	0.75	0.5	1823	0.08	0.08
1773	0.65	0.3	1873	0.07	0.04
1823	0.6				
1873	0.35	0.2			

Slag Atlas (Allibert et al., 1995)

Temp. (K)	15-Al ₂ O ₃ ; 25-CaO; 60-SiO ₂	24-CaO; 29-Fe ₂ O ₃ ; 47-SiO ₂	49.5-CaO; 10-Fe ₂ O ₃ ; 40.5-SiO ₂	20-Na ₂ O; 80-SiO ₂
1273	1.7	1.75	2.1	1.1
1373	1.6	1.6	2	0.6
1473	1.5	0.75	1.55	0.25
1573	1.25	0.45	1	0.1
1673	0.8	0.25	0.5	
1773		0.2	0.35	

Table A.14

The electrical conductivity (σ) of various lunar regolith simulants (all values are in S/m).

Derived from Ducret et al. (2002) (25% CaO, 25% MgO, 50% SiO ₂)					From Carroll (1983)		
Temp. (K)	+0% FeO	+5% FeO	+10% FeO	+15% FeO	Temp. (K)	Fe-rich Basalt	Anorthite
1667	8.6	14.2	19.2	30.1	1473	8	1.3
1695	10.5	16.5	22.3	35.0	1523	11.5	2
1724	11.6	19.2	24.7	40.7	1573	15	3.3
1754	15.0	21.2	28.7	44.9	1623	22	4.5
1786	16.5	24.7	31.7	49.7	1673	30	6
1818	20.2	28.7	36.8	54.9	1723	43	9
1835	22.3	30.1	38.7	57.7			
1852	22.8	33.3	42.7	60.7			
1887	27.3	38.7	47.2	67.0			
1923	33.3	47.2	54.9	77.9			

Derived from Rai (1977)				Derived from Haskin et al. (1992)		
Temp. (K)	Tholeiitic Basalt	Temp. (K)	Alkalic Basalt	Mineral	Temp. (K)	σ (S/m)
1173	0.2	1373	0.6	Diopside (“Diop”) [CaMgSi ₂ O ₈]	1693	6
1373	1.0	1413	2.5	Diop + 0.5% FeO	1693	25
1508	5.6	1448	3.2	Diop + 5% FeO	1693	45
1523	7.9	1473	3.5	Diop + 20% Al ₂ O ₃	1693	5
1667	10.0	1510	4.0	80 Ap15–20 Ilm	1698	175
1773	18.6	1639	10.0	Apollo 15 Mare Analog (“Ap15”)	1698	50
		1773	15.8	50% Ap15		
				50% Ilmenite	1823	475
				Anorthite	1823	9

Table A.15

The regression coefficients for the low-temperature (top section) and high-temperature (bottom section) Gibbs Free Energy and Enthalpy of Formation fits shown in Eqs. (12) and (13). The maximum (minimum) temperature for the low (high) temperature data is shown on the right.

Low temperature fits						
Specie	a_G	b_G	c_G	a_H	b_H	Max Temp. (K)
K ₂ O	−746.0	−0.0820	0.5436	−742.1	0.0333	1000
Na ₂ O	−766.9	−0.1132	0.5769	−767.6	0.0512	1100
P ₂ O ₅	−1165	−0.0030	0.3327	−1164	0.0015	1100
FeO	−497.9	−0.0074	0.1243	−500.8	0.0066	1800
Fe ₂ O ₃	−552.2	−0.0253	0.2538	−551.1	0.0093	1800
Cr ₂ O ₃	−678.6	−0.0122	0.1839	−676.9	0.0031	2100
SiO ₂	−906.3	−0.0171	0.2301	−906.5	0.0078	1600
TiO ₂	−896.7	−0.0174	0.2152	−899.0	0.0104	1900
Al ₂ O ₃	−1074	0.0264	0.1140	−1073	−0.0131	1350
MgO	−1056	0.0375	0.0528	−1055	−0.0186	1300
CaO	−1104	0.0361	0.0421	−1104	−0.0154	1700

High temperature fits						
Specie	a_G	b_G	c_G	a_H	b_H	Min Temp. (K)
K ₂ O	−1182	−0.3444	1.753	−1184	0.1517	1000
Na ₂ O	−1196	−0.2028	1.218	−1196	0.0878	1100
P ₂ O ₅	−1287	−0.0521	0.5866	−1286	0.0221	1100
FeO	−522.9	−0.0130	0.1561	−522.9	0.0056	1800
Fe ₂ O ₃	−552.5	0.0026	0.1632	−552.4	−0.0011	1800
Cr ₂ O ₃	−728.6	−0.0304	0.2684	−728.6	0.0132	2100
SiO ₂	−974.5	−0.0453	0.3612	−974.3	0.0196	1600
TiO ₂	−913.6	−0.0318	0.2711	−913.5	0.0137	1900
Al ₂ O ₃	−1154	−0.1110	0.6038	−1154	0.0481	1350
MgO	−1412	−0.1128	0.7845	−1409	0.0479	1300
CaO	−1494	−0.0903	0.6732	−1491	0.0377	1700

References

- Allibert, M., Gaye, H., Geiseler, J., Janke, D., Keene, B.J., Kirner, D., Kowalski, M., Lehmann, J., Mills, K.C., Neuschütz, D., Parra, R., Saint-Jours, C., Spencer, P.J., Susa, M., Tmar, M., Woermann, E., 1995. *Slag Atlas*. Verlag Stahleisen, GmbH.
- Arndt, J., Flad, K., Feth, M., 1979. Radiative cooling experiments. In: *Lunar and Planetary Science Conference Proceedings*, vol. 10, pp. 355–373.
- Badescu, V., 2012. *Moon: Prospective Energy and Material Resources*. Springer.
- Balasubramaniam, R., Gokoglu, S., Hegde, U., 2010. The reduction of lunar regolith by carbothermal processing using methane. *Int. J. Miner. Process.* 96 (1), 54–61.
- Basu, A., Riegsecker, S., 2000. Modal mineralogic distribution in the regolith at apollo landing sites. *J. Geophys. Res. Planets* 105 (E2), 4361–4368, 1991–2012.
- Carroll, W.F., 1983. Research on the use of space resources. *JPL Publ.*, 83–136.
- Chase, M. W., 1998. *Nist-janaf Thermochemical Tables*, fourth ed. Journal of Physical and Chemical Reference Data Monographs.
- Colozza, A.J., 1991. Analysis of lunar regolith thermal energy storage. NASA STI/Recon Technical Report N, 92, 14480.
- Colson, R.O., Haskin, L.A., 1990. Lunar oxygen and metal for use in near-earth space: Magma electrolysis. In: *NASA Space Engineering Research Center for Utilization of Local Planetary Resources*.
- Crawford, I.A., 2014. Lunar resources: a review. *arXiv preprint. arXiv: 1410.6865*.
- Cremers, C., 1975. Thermophysical properties of apollo 14 fines. *J. Geophys. Res.* 80 (32), 4466–4470.
- Ducret, A., Khetpal, D., Sadoway, D.R., 2002. Electrical conductivity and transference number measurements of feo-caomgo-sio2 melts. In: *Electrochemical Society Meeting*, Philadelphia, pp. 347–353.
- Fagents, S.A., Rumpf, M.E., Crawford, I.A., Joy, K.H., 2010. Preservation potential of implanted solar wind volatiles in lunar paleoregolith deposits buried by lava flows. *Icarus* 207 (2), 595–604.
- Fulcher, G.S., 1925. Analysis of recent measurements of the viscosity of glasses. *J. Am. Ceram. Soc.* 8, 339–355.
- Haskin, L.A., Colson, R.O., Lindstrom, D.J., Lewis, R.H., Semkow, K. W., 1992. Electrolytic smelting of lunar rock for oxygen, iron, and silicon. In: *Lunar Bases and Space Activities of the 21st Century*, vol. 1, pp. 411–422.
- Heiken, G.H., Vaniman, D.T., French, B.M., 1991. *The Lunar source-book: a user's guide to the Moon*. CUP Archive.
- Hemingway, B., Robie, R., Wilson, W., 1973. Specific heats of lunar soils, basalt, and breccias from the apollo 14, 15, and 16 landing sites, between 90 and 350 k. In: *Lunar and Planetary Science Conference Proceedings*, vol. 4, pp. 2481.
- Horai, K.-I., 1981. The effect of interstitial gaseous pressure on the thermal conductivity of a simulated apollo 12 lunar soil sample. *Phys. Earth Planet. Inter.* 27 (1), 60–71.
- Kallerud, M., Nguyen, B., Paladin, T., Wilson, A., 2011. In-situ resource utilization: Investigation of melted lunar regolith simulant jsc-1a. In: *Proceedings of the Wisconsin Space Conference*.
- Kang, Y., Morita, K., 2006. Thermal conductivity of the cao-al2o3-sio2 system. *ISIJ Int.* 46 (3), 420–426.
- Keihm, S., Langseth, M., Jr., 1973. Surface brightness temperatures at the apollo 17 heat flow site: thermal conductivity of the upper 15 cm of regolith. In: *Lunar and Planetary Science Conference Proceedings*, vol. 4, pp. 2503.
- Kojitani, H., Akaogi, M., 1995. Measurement of heat of fusion of model basalt in the system diopside–forsterite–anorthite. *Geophys. Res. Lett.* 22 (17), 2329–2332.
- Langseth Jr, M.G., Clark Jr, S.P., Chute Jr, J.L., Keihm, S.J., Wechsler, A.E., 1972. The apollo 15 lunar heat-flow measurement. *The Moon* 4 (3–4), 390–410.
- Linne, D.L., 2010. Employing isru models to improve hardware design. In: *Proceedings of 48th AIAA Aerospace Sciences Meeting Including the New Horizons Forum and Aerospace Exposition*.
- Lucey, P.G., Blewett, D.T., Jolliff, B.L., 2000. Lunar iron and titanium abundance algorithms based on final processing of clementine ultra-violet–visible images. *J. Geophys. Res. Planets* 105 (E8), 20297–20305, 1991–2012.
- Mueller, R.P., Townsend, I.I., Mantovani, J.G., Metzger, P.T., 2010. Evolution of regolith feed systems for lunar isru o2 production plants. In: *48th AIAA Aerospace Sciences Meeting Including the New Horizons Forum and Aerospace Exposition*.
- Olhoeft, G., Frisillo, A., Strangway, D., Sharpe, H., 1974. Temperature dependence of electrical conductivity and lunar temperatures. *The Moon* 9 (1–2), 79–87.
- Planck, M., 1914. *The theory of heat radiation*. Masius (Blackiston, Philadelphia, 1914), Sec. 164, 175.
- Rai, C.S., 1977. *Electrical and Elastic Properties of Basalts and Ultramafic Rocks as a Function of Saturation, Pressure and Temperature* (PhD thesis).
- Richet, P., Bottinga, Y., 1986. Thermochemical properties of silicate glasses and liquids: a review. *Rev. Geophys.* 24 (1), 1–25.
- Richter, S.W., 1992. Experimental determination of in situ utilization of lunar regolith for thermal energy storage. Technical report, SAE Technical Paper.
- Rumpf, M.E., Fagents, S.A., Crawford, I.A., Joy, K.H., 2013. Numerical modeling of lava-regolith heat transfer on the moon and implications for the preservation of implanted volatiles. *J. Geophys. Res. Planets* 118 (3), 382–397.
- Schiefelbein, S.L., Sadoway, D.R., 1997. A high-accuracy, calibration-free technique for measuring the electrical conductivity of molten oxides. *Metall. Mater. Trans. B* 28 (6), 1141–1149.
- Schreiner, S.S., Sibille, L., Dominguez, J.A., Hoffman, J.A., Sanders, G.B., Sirk, A.H., 2015. Development of a molten regolith electrolysis reactor model for lunar in-situ resource utilization. In: *AIAA SciTech Conference – 8th Symposium on Space Resource Utilization*.
- Sibille, L., Dominguez, J.A., 2012. Joule-heated molten regolith electrolysis reactor concepts for oxygen and metals production on the moon and mars. In: *50th AIAA Aerospace Sciences Meeting including the New Horizons Forum and Aerospace Exposition*. AIAA 2012-0639.
- Sirk, A.H., Sadoway, D.R., Sibille, L., 2010. Direct electrolysis of molten lunar regolith for the production of oxygen and metals on the moon. *ECS Trans.* 28 (6), 367–373.
- Snyder, D., Gier, E., Carmichael, I., 1994. Experimental determination of the thermal conductivity of molten camgsi2o6 and the transport of heat through magmas. *J. Geophys. Res. Solid Earth* 99 (E8), 15503–15516, 1978–2012.
- Solomon, A., Alexiades, V., Jacobs, G., Naney, M., Olszewski, M., 1992. Latent heat thermal energy storage for lunar oxygen production. In: *Fluid Mechanics Phenomena in Microgravity*; ASME Winter Annual Meeting, vol. 1, pp. 8–13.
- Standish, E., 2010. Design of a molten materials handling device for support of molten regolith electrolysis (PhD thesis). The Ohio State University.
- Stebbins, J., Carmichael, I., Moret, L., 1984. Heat capacities and entropies of silicate liquids and glasses. *Contrib. Mineral. Petrol.* 86 (2), 131–148.
- Stoeser, D., Rickman, D., Wilson, S., 2010. Design and specifications for the highland regolith prototype simulants NU-LHT-1M and-2M, Citeser.
- Tamman, G., Heese, W., 1926. Die abhängigkeit der viscosität von der temperatur bei unterkühlten flüssigkeiten. *Z. Anorg. Allg. Chem.* 156, 245–257.
- Taylor, L.A., Carrier III, W.D., 1992. Production of oxygen on the moon: which processes are best and why. *AIAA J.* 30 (12), 2858–2863.

- Vila, J., Gines, P., Pico, J., Franjo, C., Jimenez, E., Varela, L., Cabeza, O., 2006. Temperature dependence of the electrical conductivity in emim-based ionic liquids: evidence of vogel–tamman–fulcher behavior. *Fluid Phase Equilib.* 242 (2), 141–146.
- Vogel, H., 1925. *Phys. Z. J. Am. Chem. Soc.* 22, 645–646.
- Wakabayashi, S., Matsumoto, K., 2006. Development of slope mobility testbed using simulated lunar soil. JAXA Research and Development Memorandum.
- Watson, K., 1964. I. The thermal conductivity measurements of selected silicate powders in vacuum from 150–350 k, ii. An interpretation of the moons eclipse and lunation cooling as observed through the earths atmosphere from 8–14 microns. California Institute of Technology.
- Zacny, K., Mueller, R., Galloway, G., Craft, J., Mungas, G., Hedlund, M., Fink, P., 2009. Novel approaches to drilling and excavation on the moon. *AIAA SPACE Conference & Exposition*, 6431–6443.